Synthesis of photoluminescent β-Ga$_2$O$_3$ nanostructures using electrospinning method, and control of length-diameter ratio by calcination heating rates

Aline Varella Rodrigues[1] · **Naira Linhares Sabino[1]**

Abstract

Nanofiber precursors of PVP-Ga(NO$_3$)$_3$ were synthesized through the electrospinning technique, and monoclinic β-Ga$_2$O$_3$ patterns were later obtained through the calcination method. During the annealing process, the nanofibers' pores decreased, and their lengths were uniform up to several micrometers due to the surface-to-core extension that comprises the crystallization through Ostwald ripening process. Synthesis on the structure and morphology of materials were investigated using scanning and transmission electron microscopy equipped with an energy dispersive spectrometer, X-ray diffraction, Raman and Fourier-transform infrared (FTIR) spectroscopies. The β-Ga$_2$O$_3$ optical properties disclosed very broad and intense photoluminescence emission spectrum in the blue region of the wavelength, whose driving force was the presence of oxygen vacancies in the structures. Two types of Ga^{3+} ions (GaO$_6$ octahedral and GaO$_4$ tetrahedral chains) were demonstrated to come from different vibrations of Ga–O bonds in the Raman and FTIR spectra. And Ga^{3+}–CO adducts formed on coordinatively Ga^{3+} ion located at edges and corners of β-Ga$_2$O$_3$ crystallites. Thus, successful results of this work included the control of length-diameter ratio by calcination heating rates, as well as the broad blue emission band, representing a strong potential of β-Ga$_2$O$_3$ materials in optoelectronic applications.

1 Introduction

Electrospinning is considered a method which is versatile for generating long fibers, ranging from dozens of nanometers to micrometers. This technique enables to manipulate the nanofiber diameter, composition, and tune their high surface area to volume ratio and their porosity [1]. Through it, the materials growth has been described to be driven by aggregation and continuous growth of individual crystallites. Examples of these materials can be found as inorganic synthesis systems in solutions, with polymers as surface protection agents and the enhancement of aggregation and intern-particle interaction [2]. Regarding the synthesis of one-dimensional (1 D) materials with different compositions, the electrospinning is simpler, convenient and cost-effective than other methods, like carbothermal reduction,

metal-catalyzed vapor–liquid–solid, hydrothermal, and template-based methods [1, 3, 4]. Polymer, polymer/inorganic, composites, and inorganic nanofiber are related to be the usual materials developed through the electrospinning technique [5].

Concerning the light emitters, waveguides and light detectors, materials as nanorods, nanowires and nanofibers are often desired [4]. Due to unique electronic, optoelectronic and mechanical properties, their 1 D nanomaterials have attracted great attention. One example is the Ga$_2$O$_3$ material, which has wide band gap, with a value of about 4.9 eV. This transparent oxide semiconductor, with a monoclinic phase in the visible spectrum to ultraviolet, have innumerous applications, specially within the optoelectronic devices, field effect transistors and gas sensors [6, 7]. The presence of both cation and anion vacancy sites are the responsible for the unique PL properties [8], as well as the 1 D, mesoporous and hierarquical structures with large surface area to volume ratio [9, 10].

The β-Ga$_2$O$_3$ monoclinic structure is the most thermodynamically stable phase, having other polymorphic phases (α-, γ-, δ- and ε-) ultimately transformed into β- through the calcination processes [11]. Several β-Ga$_2$O$_3$ physical

✉ Aline Varella Rodrigues
  alinevarellarodrigues@gmail.com

[1] Department of Physical-Chemistry, UNESP University, Rua Prof. Francisco Degni, 55, Bairro Quitandinha, Araraquara, SP CEP 14800-060, Brazil

properties are originated from the native point defects. The existence of shallow donor states is led by either oxygen vacancies or large number of dopants, providing the electrical conductivity source of the n-type β-Ga_2O_3. Its large surface to volume ratio also provides interesting physical behaviors due to the large surface that interacts with the surrounding environment and promotes the desired surface-states. For the purpose of obtaining superior physical properties than the ones from bulk materials arisen from the quantum effects, nanostructured Ga_2O_3 are usually required [12].

It is reported that the electrospinning technology provides excellent processability of polymeric materials [13]. Within the photoluminescence issue, however, few researches describe the studies of the β-Ga_2O_3 nanofibers applying the electrospinning technique: strong emissions could be appeared with large band widths from 400 to 750 nm, depending on the defects created into the matrix during the temperature annealing processes [3, 14]. Besides the β-Ga_2O_3 nanofibers can exhibit smaller fiber diameter with decreasing solvent, e.g. ethanol, which is attributed to the sufficient time of electrostatic force to pull and stretch the polymer strand before reaching the fiber collector. It is also known that the dielectric constant of the solution leads to higher Coulombic repulsion force, which decreases the diameter of formed fiber via increased stretching forced exerted on the charged jet segment [7]. All that findings could facilitate the exploration of the desired light-emitting materials. Therefore, the development of the related materials is the main goal of this work, aiming their intense PL for achieving targeted optical properties, once the nanoscale gallium oxide is related to have considered conduction and optical properties for being applied in optoelectronic devices.

2 Materials and methods

The nanofibers of β-Ga_2O_3 materials were developed through the electrospinning followed by calcinations processes [3, 4]. As-prepared solutions were carried out by dissolving 15 wt% poly(vinyl pyrrolidone) (PVP, Sigma-Aldrich, $M_w \approx 1,300,000$) in the mixed distilled water and ethanol with the weight ratio of 1:1, keeping the vigorous stirring for 3 h at room temperature. Into the solution, 0.1 g $Ga(NO_3)_3 \cdot xH_2O$ (Sigma-Aldrich) was added, keeping the new solution in the vigorous stirring for 10 h, achieving the desired viscosity for the electrospinning technique.

The solution was inject into a plastic syringe equipped with stainless needle (18 inch), which was connected with a peristaltic pump to insure the flow rate of the solution at 0.035 mL min^{-1}. The connected stainless needle was linked to a high voltage–power supply, and a plate of aluminum foil was placed with a distance of 15 cm from the needle tip. A high electric voltage of 20 kV was applied between the stainless needle and the collector, and the precursors were obtained on the aluminum foil as dense mats. The as-prepared nanofibers were dried at 70 °C for 5 h and calcined at 900 °C in air for 1 h in order to obtain the β-Ga_2O_3 fine nanofibers. The temperature heating rate was varied (1, 5 and 10 °C/min) aiming fine nanofibers.

The field emission gun scanning electron microscope (FEG-SEM; JEOL, model JSM-7500F) equipped with an energy dispersive spectrometer (EDS) was used to analyze the morphology of the produced structures, and the transmission electron microscope (TEM; PHILIPS, model CM200) allowed us to correlate the morphology and structural characteristics of β-Ga_2O_3 nanofibers.

The crystallinity and phase of the synthesized materials were analyzed by the X-ray diffraction (XRD; RIGAKU RINT-2000) using Cu $K\alpha$ radiation at a scan rate of 5 °C/min, with 2 θ from 7 to 90° (D/teX Ultra; PSD).

The micro-Raman spectrum was measured using a 632.8 nm laser source (Horiba Jobin–Yvon, model Lab RAM HR) equipped with Raman microscopy (Horiba Jobin–Yvon´s confocal Raman microscope). The Fourier-transform infrared (FTIR) spectra were recorded in the range from 4000 to 400 cm^{-1} (BRUCKER, model VERTEX 70).

Photoluminescence properties were studied using the excitation wavelength of 325 nm (Horiba Jobin–Yvon, model Fluorolog-3 FL3-122). Emission spectra were recorded in the range of 370–640 nm.

3 Results and discussion

PVP/$Ga(NO_3)_3$ nanofibers were obtained using the electrospinning technique. Burning organic components by annealing treatment in air, the β-Ga_2O_3 nanofibers could be formed. Due to the fact that the PVP is decomposed completely at approximately 450 °C, and a specific phase of the final product was desired, the annealing temperature at 900 °C was applied. The FEG-SEM images (Fig. 1a–c) depicted different nanofibers' diameters, which used different heating rates, realizing that thinner diameter were formed at lower rate value [3, 13].

As it is shown in Fig. 1a–c, pores appeared along the nanofibers. The pores decreased at slower heating rate, and the length was uniform up to several micrometers due to the surface-to-core extension [10], which is so-called reversed crystal growth mechanism that comprises the crystallization from the surface to core through Ostwald ripening process. The surface-to-core extension is related to participate of a large number of inorganic compounds crystallization, such as zeolites, perovskites, metal, and metal oxides [2]. A scheme of the reversed crystal growth is illustrated in Fig. 1d.
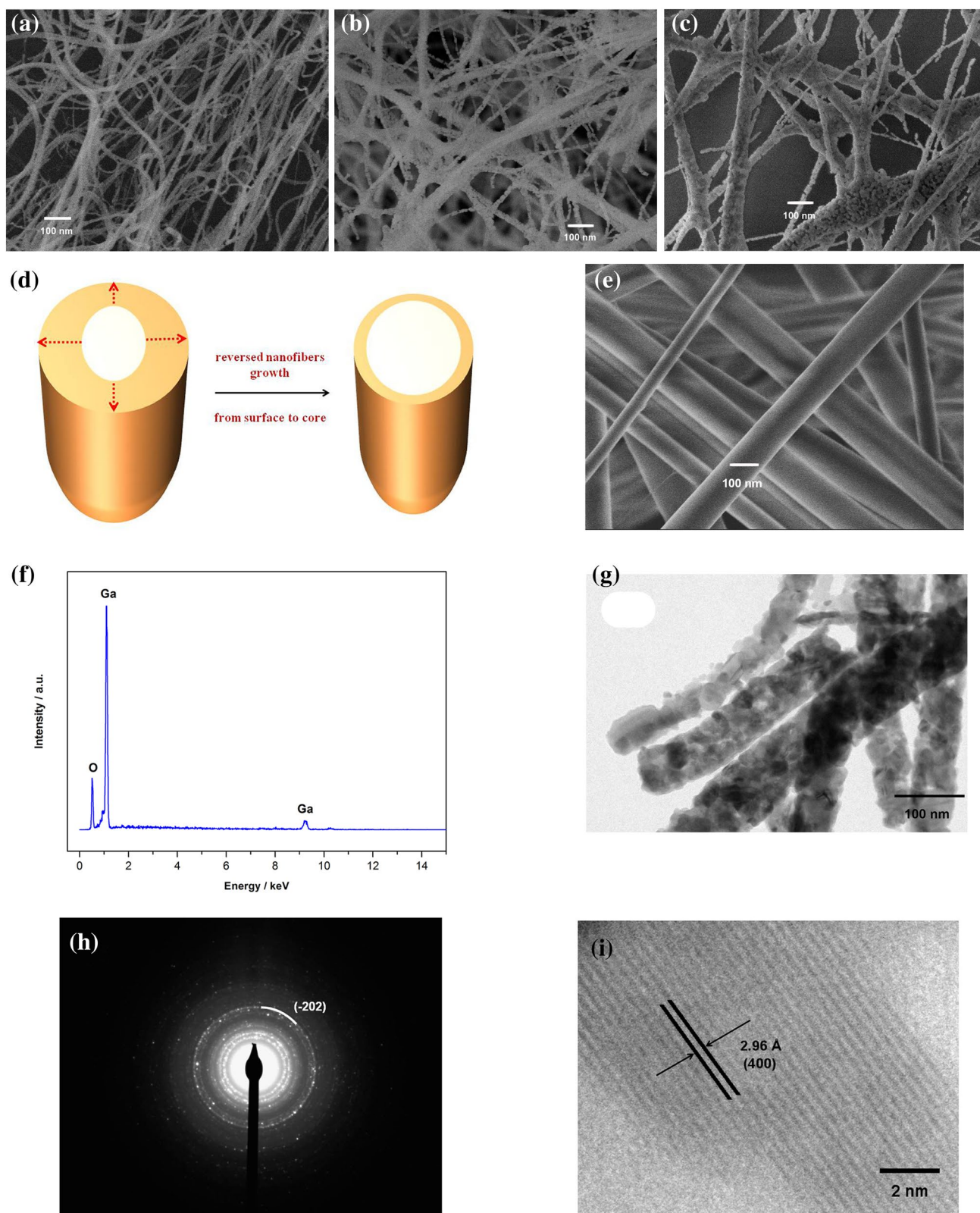
Fig. 1 FEG-SEM images of β-Ga$_2$O$_3$ nanofibers synthesized at 1 °C (**a**), 5 °C (**b**), 10 °C (**c**) per minute, and later calcined at 900 °C; reversed crystal growth (**d**); FEG-SEM image of the precursor annealed at 70 °C (**e**); EDS (**f**); TEM (**g**); SAED (**h**); and HRTEM that illustrates the atomic structure in (−202) crystal plane (**i**) of the gallium oxide produced at 1 °C
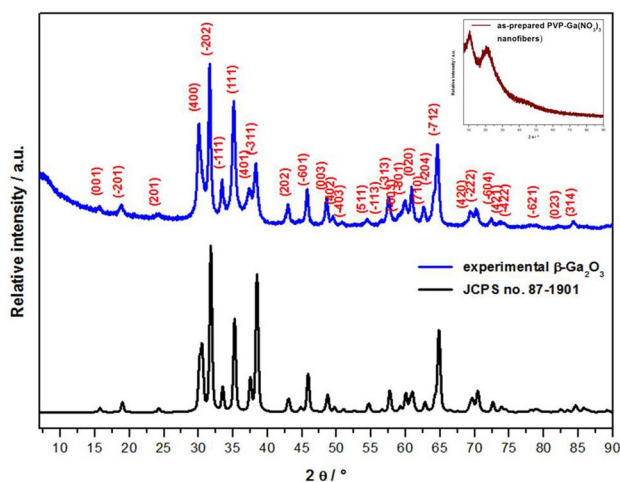
Fig. 2 Standard (JCPS card no. 87-1901) and experimental XRDs of β-Ga_2O_3, as well as the as-prepared nanofibers XRD

Comparing the nanofibers before and after being annealed at the higher temperature, it is observed smaller length-diameter ratio for the nanofibers formed at 70 °C (Fig. 2e), with the PVP covering the $Ga(NO_3)_3 \cdot xH_2O$ material. At higher annealing temperature as 900 °C, the fiber diameters decreased, changes took place on the surfaces due to the evaporation of ethanol, and the degradation of PVP and decomposition of $Ga(NO_3)_3$ occurred, as previously described in the literature [15]. FEG-SEM images of β-Ga_2O_3 calcined at 1 °C, 5 °C and 10 °C per min are depicted in Fig. 1a–c, respectively, showing that they morphologically appeared as nanofibers, with large length-diameter ratio.

The material composition was characterized using the EDS technique, exhibiting the Ga and O peaks from the materials in analysis (Fig. 1f). One dimensionally β-Ga_2O_3 nanofibers were formed, as demonstrated. Both low-magnification TEM (Fig. 1g) and FEG-SEM images demonstrated diameters of approximately 60 nm for thinner nanofibers, which were synthesized at slower heating rate. The nanofiber nature of β-Ga_2O_3 was investigated using the SAED image (Fig. 1h). High-resolution image (HRTEM, Fig. 1i) demonstrated well-resolved lattice fringes, with a distance between each other as 2.8 Å, corresponding to the interplanar spacing value of (− 202) atomic plane of β-Ga_2O_3 [16], in agreement with the literature (JCPS no. 87-1901) and the experimental results, appearing as one of the stronger XRD peak intensities.

After the thermal treatment, the crystallinity and phase of the materials synthesized were analyzed using the XRD equipment, which demonstrated that the nanofibers were monoclinic structures [17]. The diffraction peaks of the β-Ga_2O_3 nanofibers were obtained and fully indexed in the monoclinic structure (JCPS no. 87-1901), as depicted in

Fig. 2, showing that the cell parameters corresponded to a = 12.2140 Å, b = 3.0371 Å, c = 5.79810 Å, and β = 103.83 Å, and the space group corresponded to C2/m. The Miller indices (hkl) of β-Ga_2O_3 were shown in the XRD plots. Other impurity phases were not detected [14]. Before the thermal treatment at high temperature, the precursor appeared in the XRD as an amorphous phase. According to L. Wang (2009), one of the diffraction peaks appeared with broad width at around $2\theta = 22°$ corresponded to the semicrytalline PVP [1], which is depicted in Fig. 2 of this work.

The PL spectrum of the β-Ga_2O_3 (Fig. 3) showed an emission band located at a maximum value of approximately 420 nm under an excitation wavelength of 325 nm at room temperature. This blue band emission has been described to come from the recombination of an electron on a donor formed by the oxygen vacancies (V_o^x) and a hole on an acceptor formed by the gallium vacancies (V_{Ga}''') or by gallium-oxygen vacancy pairs ($V_o^{..}$, V_{Ga}''')'. The holes trapped on the acceptors recombined radiatively, emitting photons around the blue region of the wavelength. Usually, high temperatures of calcinations originate emissions in the blue range of the wavelength due to the presence of oxygen vacancies, which are easily formed because of higher surface to volume ratio. The asymmetry of the emission band can also be explained by the electron–phonon interactions [5, 18].

Unlike it was not found here in this work, another sort of emission could be present in matrixes of Ga_2O_3: recent researches have described a red light emission that came from the nitrogen absorbed into the host lattice. In this case, Ga_2O_3 particles synthesized in air were doped with N and post-annealed in ammonia atmosphere with different nitrogen doping concentrations, whose photoluminescence spectra showed an emission band in the red range of the wavelength. The particles prepared without nitrogen
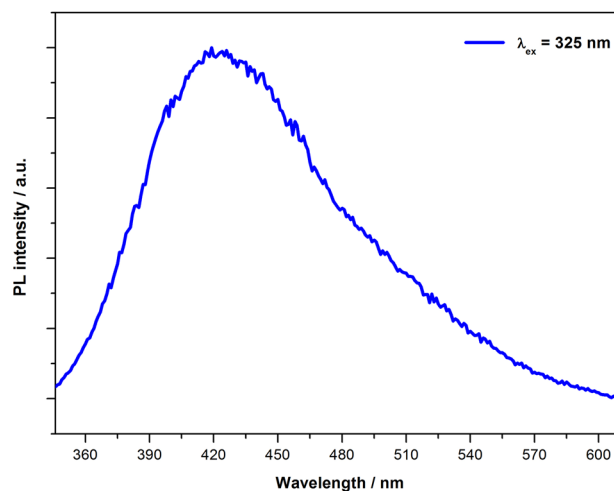

Fig. 3 PL emission spectra of β-Ga_2O_3 nanofibers at room temperature using an excitation wavelength of 325 nm

doping presented no red light emission [18]. The red light has also appeared after Ga_2O_3 samples were annealed in oxygen ambient environment at high temperatures [19]. N–N bond lengths and N–N stretching frequencies of N-complexes higher activation is also found through the enzymatic reduction of ammonia, another possible process that applies enzyme nitrogenase to fixes dinitrogen into the matrix using specialized catalysts, high pressure and high temperature [20, 21]. It can be inferred that intrinsic emission band comes from the recombination of an electron trapped on a donor due to the oxygen vacancy and a hole trapped on an acceptor due to the nitrogen doping. The electron trapped on the donor, induced by the nitrogen doping, recombine radiatively, emitting photons around the red region of the wavelength [18, 19]. A representative scheme of the PL mechanism for blue, UV, green and red emissions is depicted in Fig. 4. Through the energy band diagram, the origin of possible emissions is shown.

Generated by the recombination of an electron trapped on a donor due to V_o^x and a hole trapped on an acceptor due to N impurity from the atmosphere, a red emission is observed. The N impurity enables a creation of a deep acceptor level inside the band gap. This level lies near the middle of the band gap [22]. Therefore, the main recombination channel occurs via defect level inside the band gap. Thus, created electrons, composed by holes, are firstly relaxed to the band edges, being trapped by the defect levels inside the band gap, and the carriers are recombined, producing a photon with the energy $h\nu_1$ that is inferred to the red emission [23]. In case of blue emission, this band can be originated by V_{Ga}''', V_o^x, and $(V_o^{..}, V_{Ga}''')'$ in Ga_2O_3. The blue emission is described to come from the recombination of a donor–acceptor pair (DAP) through a tunneling process. And the UV emission is reported to be originated by the recombination of self-trapped excitons, which are created when an electron at the donor level (formed by V_o^x) is captured by a hole at the acceptor level [formed by V_{Ga}''' or $(V_o^{..}, V_{Ga}''')'$] [22, 24].
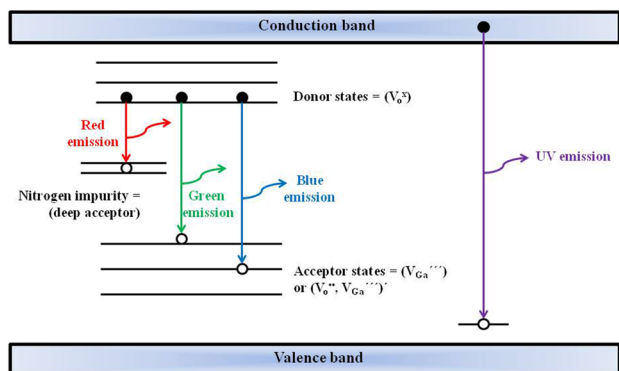
Besides the blue and the green emissions generation can mainly be associated with V_{Ga}''', $(V_o^{..}, V_{Ga}''')'$, and oxygen interstitials. The green PL emission can come from the neutral oxygen interstitial defects, and from isolated gallium vacancies (octahedral site with -2 charge state or tetrahedral site with -1 charge state) [25].

Moreover, researches have related different emissions of the Ga_2O_3 nanostructures due to different regions observed in the materials: a crystalline β-Ga_2O_3 core and an amorphous shell. The blue and yellow emissions are originated from the crystalline β-Ga_2O_3 core. In regard to the V_o^x, the UV and blue emission intensities are dependent on them: the intensity of UV-blue emission decreases as the number of V_o^x decreases. Reaction time also affects the V_o^x, consequently, the emission intensity: as long as the reaction time increases, there is an improvement of the crystallinity, which facilitates the reduction of the V_o^x concentration, decreasing the emission intensity [22, 24].

The detailed structural characterizations were studied through the analysis of micro-Raman spectrum, as depicted in Fig. 5. The Raman peaks were in a good agreement with the literature. According to the researches, a large number of defects can be detected through red-shifted peaks. The monoclinic β-Ga_2O_3 is related to belong to the space group of C_{2h} where 15 Raman modes are expected to be observed in the material vibration spectrum. The Raman peaks which appeared in this work were indexed in the calculated Raman active modes as reported in the literature (Local Density approximation) [26]. In this work, the experimental peaks at 113, 145, 169, and 200 cm^{-1} corresponded to low frequency modes, which come from the libration and translation of tetrahedral-octahedral chains. Mid-frequency modes that are located in the range of approximately 500–300 cm^{-1} correspond to the deformation of GaO_6 octahedral modes (here, the peaks were located at 320, 347, 416, and 475 cm^{-1}).
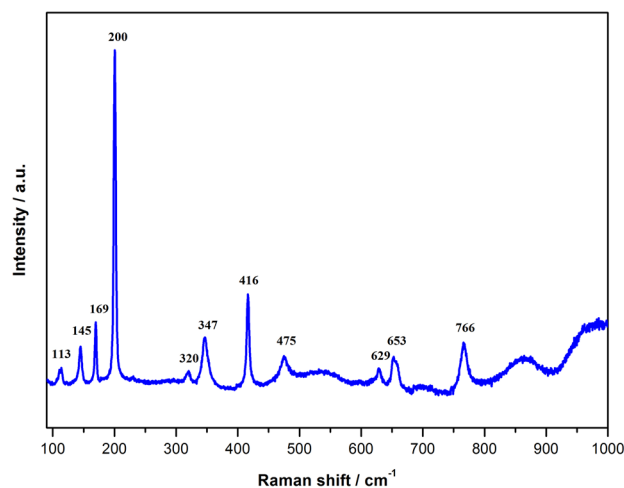

Fig. 4 Scheme of PL for β-Ga_2O_3 nanofibers: blue, UV, green and red emissions (Color figure online)

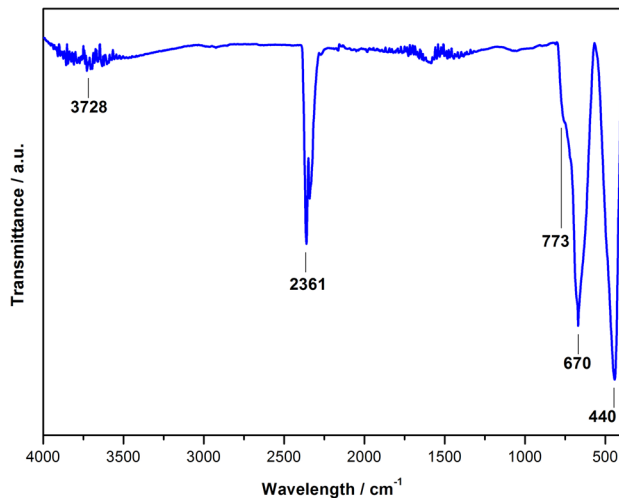**Fig. 5** Micro-Raman spectrum of β-Ga_2O_3 nanofibers

Fig. 6 FTIR spectra of β-Ga$_2$O$_3$ nanofibers

And high-frequency modes that are located in the range of approximately 770–500 cm^{-1} correspond to the stretching and bending GaO$_4$ tetrahedral modes [27, 28]. In this work, they were located at 629, 653, and 766 cm^{-1}.

Confirming the formation of crystalline β-Ga$_2$O$_3$ nanofibers and identifying any adsorbed elements on their surface, FTIR was measured from 4000 to 400 cm^{-1}, as depicted in Fig. 6. Intensities at 440 cm^{-1} and 670 cm^{-1} are inferred to be regions correspondent to Ga–O stretching vibrations from GaO$_6$ octahedra and O–Ga–O bending vibrations from GaO$_4$ tetrahedra, respectively. The region at 773 cm^{-1} corresponded to the stretching and bending vibrations of GaO$_4$ tetrahedra [29–31]. The peak at high-energy of a maximum value as 2361 cm^{-1} can be attributed to the adsorption of CO that came from the air atmosphere. According to M.R. Delgado (2003), there is a formation of Ga^{3+}–CO adducts on coordinatively Ga^{3+} ion located at edges and corners of β-Ga$_2$O$_3$ crystallites. Lateral interactions between adsorbed CO molecules occur due to the β-Ga$_2$O$_3$ has a crystal structure where the Ga^{3+} ions occupy both distorted tetrahedral and octahedral sites [32, 33]. Another weak and broad band, with a maximum at 3728 cm^{-1} is ascribed to –OH bending vibrations of H$_2$O molecules absorbed on the β-Ga$_2$O$_3$ surface, suggesting that the Ga–OH radicals could be incorporated into the gallium oxide. Both weaker regions showed hydrogen stretch modes which came from the H$_2$O adsorbed by the β-Ga$_2$O$_3$ nanofibers investigated at room temperature in air atmosphere [19, 34].

β-Ga$_2$O$_3$ nanofibers could be obtained as the final product in this proposed work, with Ga–O stretching vibrations and O–Ga–O bending vibrations appearing at 440 and 670 cm^{-1}, respectively, as depicted in Fig. 6.

In summary, broadness, intensity, and emission bands in the visible spectrum show that the materials are promising candidates for optoelectronic applications, as they were demonstrated in the literature [35].

4 Conclusions

Electrospinning was applied with successful, synthesizing nanofibers of β-Ga$_2$O$_3$ in a monoclinic structure and beta phase after thermal treatment at 900 °C for 1 h in the oven. The diameter and morphology of electrospun nanofibers were controlled by applying the temperature heating rate as 1, 5 and 10 °C/min, aiming fine nanofibers. Aging temperature and time of synthesis control the formation of oxygen vacancies, which were the driving forces of the existence of the strong blue emission. The nanofibers' pores decreased at slower heating rate, and the length was uniform up to several micrometers due to the surface-to-core extension, also called reversed crystal growth mechanism that occurred through the Ostwald ripening process. GaO$_6$ octahedral and GaO$_4$ tetrahedral chains were the two types of Ga^{3+} ions that came from different vibrations of Ga–O bonds, demonstrated in the Raman and FTIR spectra. There was also a formation of Ga^{3+}–CO adducts on coordinatively Ga^{3+} ion located at edges and corners of β-Ga$_2$O$_3$ crystallites, showed in FTIR spectrum. Thus, successful results of this work included the synthesis and the broad, intense, and visible emission in the blue range of the wavelength, representing strong potential of β-Ga$_2$O$_3$ materials for applications as light-emitting materials in optoelectronic devices.

References

1. L. Wang, Z. Hou, Z. Quan, H. Lian, P. Yang, J. Lian, Mater. Res. Bull. **44**, 1978–1983 (2009)
2. H.F. Greer, F.J. Yu, W.Z. Zhou, Sci. China **54**, 1867–1876 (2011)
3. T. Zhou, P. Chen, S. Hu, Y. Yan, W. Pan, H. Li, Ceram. Int. **42**, 6467–6474 (2016)
4. J. Zhao, W. Zhang, E. Xie, Z. Ma, A. Zhao, Z. Liu, Appl. Surf. Sci. **257**, 4968–4972 (2011)
5. J.G. Zhao, Z.X. Zhang, Z.W. Ma, H.G. Duan, X.S. Guo, E.Q. Xie, Chin. Phys. Lett. **25**, 3787–3789 (2008)
6. C. Han, W. Mao, K. Bao, H. Xie, Z. Jia, L. Ye, Int. J. Hydrog. Energy **42**, 19913–19919 (2017)
7. Y. Yoon, K.I. Han, B.H. Kim, I.G. Lee, Y. Kim, J.P. Kim, W.S. Hwang, Thin Solid Films **645**, 358–362 (2018)
8. B. Fernandes, M. Hegde, P.C. Stanish, Z.L. Mišković, P.V. Radovanovic, Chem. Phys. Lett. **684**, 135–140 (2017)
9. Y. Zhang, J. Yang, Q. Li, X. Cao, J. Cryst. Growth **308**, 180–184 (2007)
10. H. Chen, G.D. Li, M. Fan, Q. Gao, J. Hu, S. Ao, C. Wei, X. Zou, Sens. Actuators, B **240**, 689–696 (2017)
11. L. Cui, H. Wang, B. Xin, G. Mao, Appl. Phys. A **123**, 634 (2017)

12. D. Calestani, A.B. Alabi, N. Coppedè, M. Villani, L. Lazarinni, F. Fabbri, G. Salviati, A. Zappettini, J. Cryst. Growth **457**, 255–261 (2017)

13. S.J. Park, N.A.M. Barakat, K.U. Jeong, H.Y. Kim, Polym. Int. **60**, 322–326 (2011)

14. C. Sun, J. Deng, L. Kong, L. Chen, Z. Chen, Y. Cao, H. Zhang, X. Wang, in *5th Annual International Conference on Materials Science and Engineering*, vol. 275 (2017), p. 012046

15. J. Zhao, W. Zhang, E. Xie, Z. Liu, J. Feng, Z. Liu, Mater. Sci. Eng., B **176**, 932–936 (2011)

16. G. Sinha, S. Chaudhuri, Mater. Chem. Phys. **114**, 644–649 (2009)

17. H.M. Lam, M.H. Hong, C.L. Gan, T.C. Chong, in *Fifth International Symposium on Laser Precision Microfabrication*, vol. 5662 (2004), pp. 62–66

18. T. Zhang, J. Lin, X. Zhang, Y. Huang, X. Xu, Y. Xue, J. Zou, C. Tang, J. Lumin. **140**, 30–37 (2013)

19. Y. Cheng, J. Chen, K. Yang, Y. Wang, Y. Yin, H. Liang, G. Du, J. Vac. Sci. Technol., B **32**, 03D119 (2014)

20. S. Hinrichsen, H. Broda, C. Gradert, L. Soencksen, F. Tuczek, Annu. Rep. Prog. Chem. Sec. A **108**, 17–47 (2012)

21. B.M. Flöser, F. Tuczek, Coord. Chem. Rev. **345**, 263–280 (2017)

22. S. Kumar, V. Kumar, T. Singh, A. Hähnel, R. Singh, J. Nanopart. Res. **16**, 2189 (2014)

23. G. Pozina, M. Forsberg, M.A. Kaliteevski, C. Hemmingsson, Sci. Rep. **7**, 42132 (2017)

24. J.M. Jeong, Y.J. Kwon, H.Y. Cho, H.G. Na, H.W. Kim, J. Ceram. Process. Res. **15**, 428–432 (2014)

25. C. Liu, Y. Berencén, J. Yang, Y. Wei, M. Wang, Y. Yuan, C. Xu, Y. Xie, X. Li, S. Zhou, Semicond. Sci. Technol. **33**, 095022 (2018)

26. A. Khan, S.N. Khan, W.M. Jadwisienczak, M.E. Kordesch, Sci. Adv. Mater. **1**, 236–240 (2009)

27. I. Nowak, M. Misiewicz, M. Ziolek, A. Kubacka, V.C. Coberán, B. Sulikowski, Appl. Catal. A **325**, 328–335 (2007)

28. S. Kumar, C. Tessarek, S. Christiansen, R. Singh, J. Alloys Compd. **587**, 812–818 (2014)

29. Y. Quan, D. Fang, X. Zhang, S. Liu, K. Huang, Mater. Chem. Phys. **121**, 142–146 (2010)

30. K. Girija, S. Thirumalairajan, G.S. Avadhani, D. Mangalaraj, N. Ponpandian, C. Viswanathan, Mater. Res. Bull. **48**, 2296–2303 (2013)

31. H.J. Bae, T.H. Yoo, Y. Yoon, I.G. Lee, J.P. Kim, B.J. Cho, W.S. Hwang, Nanomaterials **8**, 594 (2018)

32. M.R. Delgado, C.O. Areán, Mater. Lett. **57**, 2292 (2003)

33. C.O. Areán, A.L. Bellan, M.P. Mentruit, M.R. Delgado, G.T. Palomino, Microporous Mesoporous Mater. **40**, 35 (2000)

34. H. Xiao, H. Pei, W. Hu, B. Jiang, Y. Qiu, Mater. Lett. **64**, 2399–2402 (2010)

35. A.V. Rodrigues, M.O. Orlandi, Ceram. Int. **45**, 5023–5029 (2019)